Journal of Materials Research and Technology 31 (2024) 3480–3488

Contents lists available at ScienceDirect

Journal of Materials Research and Technology

journal homepage: www.elsevier.com/locate/jmrt

Toward submicron inkjet-printed ZnO microdots with suppressed coffee-ring effect via controlled drying conditions for potential solar cell applications

Kyungsik Kim [a], Jun-ho Jang [b], Soonil Hong [c,*], Hongkyu Kang [b,**], Jinho Lee [a,d,***]

[a] Department of Intelligent Semiconductor Engineering, Incheon National University, 119 Academy-ro, Incheon, 22012, Republic of Korea
[b] Heeger Center for Advanced Materials and Research Institute for Solar and Sustainable Energies, Gwangju Institute of Science and Technology, Gwangju, 61005, Republic of Korea
[c] Division of Advanced Materials, Korea Research Institute of Chemical Technology (KRICT), Daejeon, 34114, Republic of Korea
[d] Department of Physics, Incheon National University, 119 Academy-ro, Incheon, 22012 Republic of Korea

ARTICLE INFO

Handling editor: P-Y. Chen

Keywords:
Inkjet printing
Fluid dynamics
Marangoni flow
Coffee-ring effect
ZnO microdot arrays

ABSTRACT

The high-resolution, inkjet-printed zinc oxide (ZnO) microdot arrays with suppressed coffee-ring effect was demonstrated by investigating the correlation between drying and solidification processes. The internal microfluidic behavior of an ejected droplet and the associated drying process is geometry-dependent, which can be controlled by the temperature and surface energy of the substrate. During evaporation, droplets in contact with a wettable surface exhibit a dominant outward convective flow, resulting in a pronounced coffee-ring effect. In contrast, for droplets with minimal contact area on a substrate with low surface energy, the surface energy gradient along the relatively long thermal conducting path length reinforces the Marangoni flow, which retards the pinning of the contact line, resulting in tiny microdots with suppressed coffee-ring effect. The controlled ZnO microdots exhibit a diameter of approximately 3 μm with a thickness of 50 nm, which is one of the smallest microstructures produced by the inkjet printing method. Additionally, the integration of the ZnO microdot arrays into organic solar cells aimed to alter the light path length, leading to enhanced internal absorption. The P3HT:PCBM, PTB7-Th:PCBM, and PM6:Y6 devices with ZnO microdot arrays exhibit higher power conversion efficiencies of 3.54%, 9.04%, and 15.61% compared to reference devices of 3.38%, 8.85%, and 15.25% respectively.

1. Introduction

Inkjet printing, a versatile and cost-effective method for precisely depositing soluble functional materials, offers significant potential for various applications across electronic and optoelectronic technologies [1–5]. One of the key advantages of inkjet printing is its ability to deposit materials with high precision, enabling intricate patterning without the need for highly sophisticated lithography processes [6–8]. Unlike traditional deposition techniques, such as physical vapor deposition or spin-coating, this maskless and noncontact approach simplifies the fabrication process and reduces production costs. Moreover, inkjet printing is highly adaptable and compatible with large-area continuous processes such as roll-to-roll printing, making this technology particularly attractive for a wide range of applications in both research and industrial fields [9–12]. The scalability of this technology allows for the efficient production of electronic devices on flexible substrates, opening up new opportunities for the advancement of wearable electronics, flexible displays, and other innovative technologies [13–18].

In printed electronics, inkjet printing techniques are being actively explored beyond the use of conductive inks (e.g., metal nanowires/nanoparticles, conductive polymers, carbon nanotubes, or graphene), extending to semiconductor materials (e.g., polymers, small molecules, quantum dots, metal oxides) for solution processes [19–27]. Achieving reliable inkjet droplet formation is paramount for precise printing, necessitating consideration of rheological parameters associated with solvent properties, including vapor pressure, surface tension, and polarity [28–32]. In addition, recent advances have shed light on phenomena related to the drying process such as pinning and the coffee-ring

* Corresponding author.
** Corresponding author.
*** Corresponding author.
E-mail addresses: sihong@krict.re.kr (S. Hong), gemk@gist.ac.kr (H. Kang), jlee@inu.ac.kr (J. Lee).

https://doi.org/10.1016/j.jmrt.2024.07.084
Received 22 April 2024; Received in revised form 30 June 2024; Accepted 15 July 2024
Available online 16 July 2024

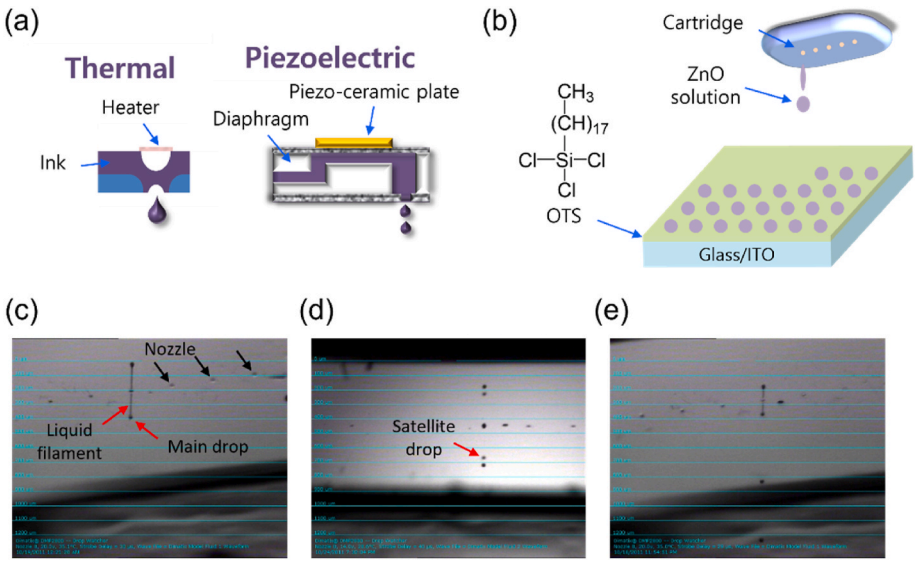

Fig. 1. (a) Schematic illustration of the jetting mechanism of an inkjet printing technique. (b) Inkjet printing of ZnO solution on surface-treated ITO substrates. Geometry of main drop and liquid filament for ejected ink with (c) high, (d) low, and (e) moderate Ohnesorge number.

effect, elucidating their influence on inkjet printing results [3,33–36]. These insights have broadened the application range of inkjet printing, facilitating the fabrication of diverse electronic components such as solar cells, LEDs, transistors, memory devices, and sensors [37–41]. In particular, inkjet printing offers unique advantages over other printing methods by enabling the creation of intricate microstructures rather than forming uniform films. This capability underscores the importance of understanding the fluidic behavior of inkjet and drying mechanisms in the design of functional device structures.

In this work, we demonstrated high-resolution zinc oxide (ZnO) microdots with suppressed coffee-ring effect by using an inkjet printing method. The sol-gel based ZnO solution system along with a high boiling point and sufficient surface tension was found to be useful for a reliable inkjet process. The analysis of the solidification behavior of ZnO droplets as a function of solution and substrate properties revealed that the nucleation-induced solidification process of inkjet-printed ZnO droplets is effectively retarded when Marangoni flow is dominant compared to capillary flow. The introduction of inkjet-printed high-resolution ZnO microdots between the electron transport layer (ETL) and the photoactive layer of an organic solar cell altered the light path due to the difference in refractive index, resulting in increased photocurrent generation.

2. Experimental section

2.1. Fabrication of inkjet-printed ZnO microdots

The ZnO microdot arrays were directly patterned via a drop-on-demand piezoelectric inkjet-printing method using a Dimatix Materials Printer (DMP-2800 Series, FUJIFILM USA). For inkjet jetting, a specially designed needle is used to inject 10 pL of solution into the cartridge (Fujifilm Dimatix Samba Cartridges, DMC-11610, 21 μm in diameter), which is then mounted in the printer. For reliable and reproducible jetting, only 1 of the 16 nozzles in the cartridge was used. The jetting conditions and parameters were optimized using Dimatix Digital Printing software. A Drop Watcher was used to investigate the generation and emission of droplets, and the jetting frequency and strobe delay were set to 4 kHz and 50 μs, respectively. A voltage of about 0.7 V was applied for the jetting of the ink based on the piezoelectric effect. The spacing between droplets was set to 100 μm. The ZnO sol-gel solution was prepared by dissolving zinc acetate dihydrate in ethylene glycol:isopropanol (1:4 vol ratio) with ethanolamine (3 vol%) and to a concentration of 1 mM and 10 mM, respectively. The ZnO heat treatment was performed at 150 °C for 10 min, after the dropped ink was completely dry.

2.2. Device fabrication

The process of fabricating organic solar cells involves the use of several materials, including indium tin oxide (ITO), polyethyleneimine (PEI), poly-3-hexylthiophene (P3HT) [6,6],-phenyl C_{61} butyric acid methyl ester (PCBM), and poly(3,4-ethylenedioxythiophene) polystyrene sulfonate (PEDOT:PSS). The device structure consists of ITO/IJ ZnO/PEI/P3HT:PCBM/PEDOT:PSS/Ag. PEI was dissolved in isopropanol at a concentration of 0.05 wt% and then spin-coated onto the substrate at 5000 rpm for 20 s P3HT:PCBM (1:1 wt ratio) was dissolved in chlorobenzene at a concentration of 20 mg ml^{-1} and spin-coated at 1200 rpm for 20 s. The samples were heat treated at 150 °C for 10 min. For PTB7-Th:PCBM devices, a solution of PTB7-Th:PCBM (1:1.5 wt ratio) in chlorobenzene:1,8-diiodooctane (97:3 vol%) was prepared at a concentration of 17 mg ml^{-1} and then spin-coated at 1200 rpm for 40 s. In the case of PM6:Y6, the solution was prepared by dissolving PM6:Y6 (1:1.2 w/w) in chloroform with a small amount of 1-chloronaphthalene for 0.5 vol% and spin-coated at 3000 rpm for 40s. PEDOT:PSS (AI 4083) was diluted with isopropanol at a 1:9 vol ratio and spin-coated on the P3HT:PCBM layer at 2000 rpm for 20 s. The MoO_3 layer was deposited to a thickness of 10 nm by thermal evaporation method. Finally, device fabrication was completed by depositing Ag to a thickness of 100 nm under high vacuum conditions.

2.3. Characterization

The microstructure of ZnO microdots was monitored using a Zeiss Axioskop 40 optical microscope equipped with a charge-coupled device camera. The 2D and 3D topographical images were obtained by atomic force microscopy in the tapping mode (XE-100, Park Systems, Inc.). Contact angles for surface energy analysis were recorded using a contact angle analyzer (Phoenix 300, SEO Co., Ltd.). The total absorption spectra of the photoactive layer were obtained through reflectance mode measurements using a UV–vis–NIR spectrophotometer system with an integrating sphere (PELA-1050), calibrated with an Ag mirror reference. The external quantum efficiency (EQE) spectra were examined using a PV Measurements, Inc. Solar cell QE measurement system. The *J–V* characteristics of the devices were measured by using a Keithley 2400

Table 1
Physical properties of solvent including viscosity, density, surface tension, and derived operating parameter Oh. Due to the very low concentration, it can be expected that there is no significant difference in the properties of the ZnO solution.

Solvent ink	Oh	Viscosity (Cp)	Density (g cm^{-3})	Surface tension (mN m^{-1})
Isopropanol	0.151	2.86	0.786	21.7
Ethylene glycol	0.548	18.38	1.113	48.2

source meter under standard illumination with an intensity of 100 mW cm^{-2}.

3. Results and discussion

In drop-on-demand inkjet printing, droplet ejection occurs through two main mechanisms: thermal and piezoelectric (Fig. 1a). Thermal inkjet printing entails the rapid vaporization of ink within chambers utilizing a heating element, thereby creating pressure pulses that expel droplets through the nozzle. Conversely, piezoelectric inkjet printing relies on piezoelectric elements to deform ink chambers, generating pressure waves that propel droplets out of the nozzle. Both approaches hinge upon meniscus formation and fluid rheology, with ink viscosity and surface tension exerting notable influence on droplet formation and print quality. While thermal printing offers simplicity and cost-effectiveness for moderate print demands, piezoelectric systems excel at high-speed and high-resolution applications owing to their precise droplet control. For reliable jetting with minimal impact on the intrinsic properties of the ejected droplets, piezoelectric inkjet printing is preferred for microelectronic applications.

Fig. 1b shows the deposition process of ZnO solution on top of the ITO substrate treated with a self-assembled monolayer (SAM). The octadecyltrichlorosilane (OTS) molecules are chemisorbed onto the ITO surface, and the mechanism is not simple, but can be explained by chemical interactions; the trichlorosilane groups of OTS react chemically with hydroxyl groups on the oxide surface, involving either ligand exchange or hydrolysis by surface OH groups. The chemically anchored OTS monolayer provides a low surface energy, as confirmed by the contact angle measurements (Fig. S1).

In fluid mechanics, the dimensionless Ohnesorge number, which represents the relative influence between the inertia and surface tension of a fluid, taking into account properties such as surface tension, density, and viscosity, provides an important guideline for understanding and predicting ink flow characteristics in inkjet printing technology [28]. Therefore, printing performance, which represents stable and reproducible ink jetting, is determined by viscosity and surface tension. The dimensionless Ohnesorge number, Oh, can be defined as

$$Oh = \frac{\mu}{\sqrt{\rho \sigma a}}$$

where μ, ρ, σ, and a are the, dynamic viscosity, density, surface tension, and characteristic dimension (usually the nozzle diameter), respectively. At high Ohnesorge number, the effect of surface tension becomes greater than viscosity, requiring a higher driving voltage to eject the droplet and forming long liquid filaments, which in turn leads to an increase in ink volume (Fig. 1c, S2 and S3). In contrast, at low Ohnesorge number, ink jetting instability due to reduced meniscus damping is observed, with the potential to generate satellite droplets (Fig. 1d and S4).

For the sol-gel synthesized ZnO, ethylene glycol and ethanolamine were used as the main solvent and stabilizer, respectively, both of which have high boiling points and sufficient surface tension to ensure reliable ink jetting without problems of ink bursting, smearing, or nozzle clogging (Figs. S5 and S6). However, the Ohnesorge number of the ZnO ink, which consists only of ethylene glycol, is rather high at 0.548, resulting in long liquid filaments at high driving voltages. This problem was alleviated by mixing with isopropanol (Oh of 0.151), which is also highly compatible with ZnO sol-gel solutions. ZnO sol-gel inks with optimized solvent ratios showed stable jetting (Fig. 1e and S7). At higher isopropanol volume fractions, weeping occurred with low Ohnesorge number. The physical properties of the solvents are provided in Table 1.

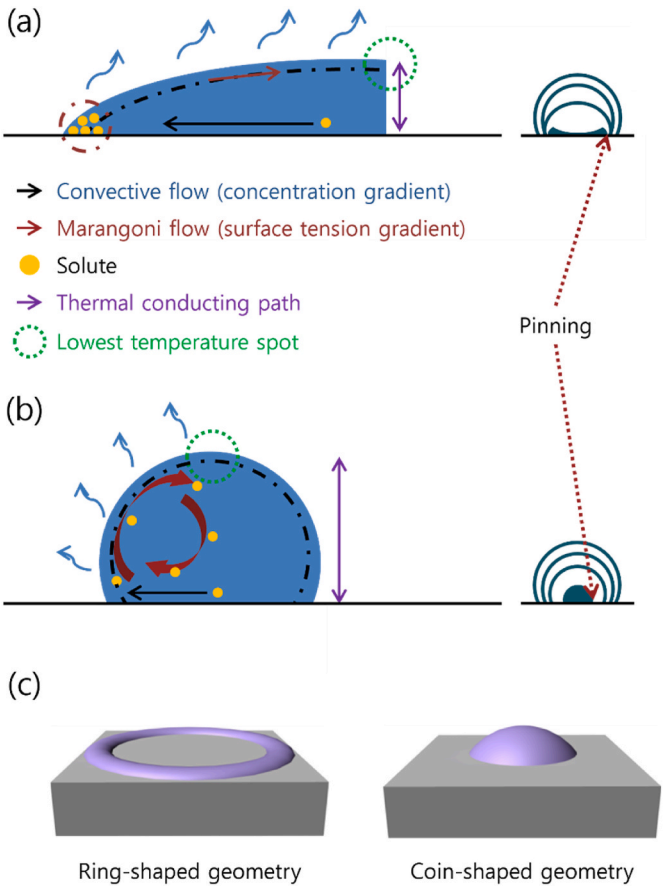

Fig. 2. Schematic representation of different drying processes for inkjet-printed droplets with (a) large and (b) small contact angles. (c) Geometry of ZnO microdots depending on drying behaviors.

For inkjet printing, drying processes such as the internal flow of droplet ink can be more important in interpreting fluid behavior than external stimuli such as shear stress or centrifugal forces, which can occur in meniscus-based printing or spin coating processes. Fig. 2 schematically illustrates the fluid flow inside a droplet with large and small contact angles and the morphology of the deposited microdots as a result of drying behavior. As the solvent evaporates, the concentration gradient causes an outward convective flow inside the droplet. Concurrently, a Marangoni flow is generated along the droplet surface between the edge and the top lowest temperature spot, which is counterbalanced by recirculation. Once the droplet is in contact with the substrate, the shape of the droplet significantly depends on the surface tension of the solvent and the surface energy of the substrate. For small contact angles, the Marangoni flow upward along the surface of the droplet is relatively weak, while convective flow transports the solute outward and accumulates around the perimeter of the droplet. When the concentration becomes higher than a critical point, solidification by nucleation occurs, which can cause the contact line to pin at the early stage of evaporation, resulting in microdots with a relatively large coffee-ring effect (Fig. 2a). Conversely, in droplets with large contact angles, the long thermal conduction paths induce an enhanced surface tension gradient due to the large temperature difference, which creates a relatively strong Marangoni flow and retards solidification (Fig. 2b). In

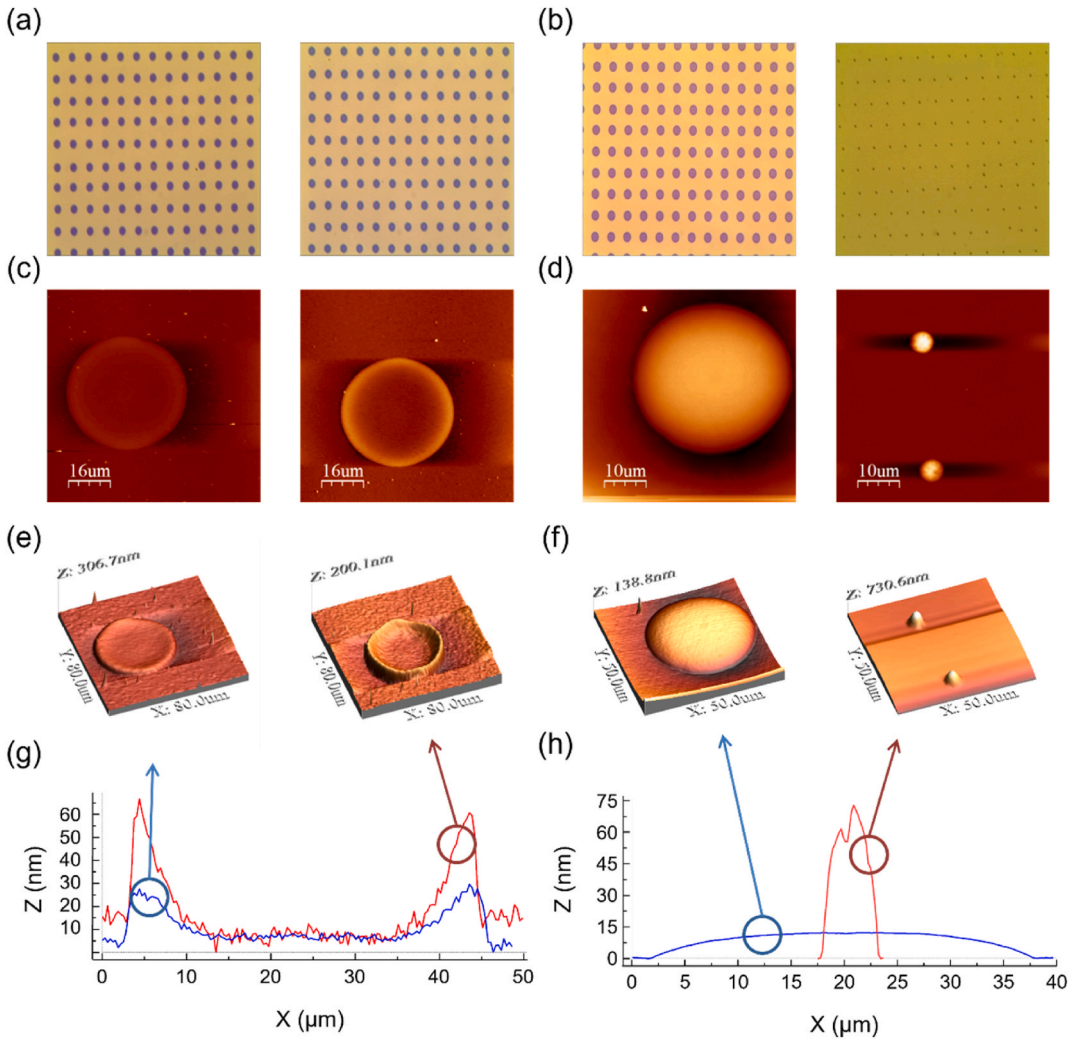

Fig. 3. (a, b) Optical microscope images of inkjet-printed ZnO microdots on the ITO substrates with (a) different temperatures of room temperature (left) and 60 °C (right), and (b) high (left) and low (right) surface energies. The corresponding (c, d) 2D and 3D (e, f) atomic force microscopy (AFM) images, and (g,h) AFM line profiles.

this case, the droplets are gradually diminished during the drying process without the contact lines being fixed, producing the smaller diameter of the deposited microdots. As shown in Fig. 2c, the resulting structural morphology of the deposited material varies, reflecting fluidic dynamics during the drying process.

Since inkjet-deposited droplets are interfaced with the substrate, factors such as the surface energy and temperature of the substrate have a significant impact on microstructure formation [42,43]. Fig. 3 provides a detailed optical and atomic force microscopy analysis of the microstructure of ZnO prepared under different deposition conditions. Fig. 3a presents the optical microscopy images of inkjet-printed ZnO microdots with room temperature and 60 °C substrates. To avoid merging droplets due to surface tension, the droplets were spaced 100 μm apart, which is sufficiently larger than the droplet ink. The deposited droplet structures showed a pronounced perimeter at both temperature conditions, with thicknesses of 25 nm and 65 nm at the edges at room temperature and 60 °C, respectively, which are thicker than the 10 nm at the center (Fig. 3g). However, as the temperature increases, the coffee-ring effect becomes stronger, which is contrary to previously reported results (Fig. 3c and **e**) [44,45]. We attribute these results to the lower surface tension of the solution at higher substrate temperatures, which results in a smaller contact angle and thus a weakening of the Marangoni flow and subsequent recirculation. In contrast to the morphological characteristics, the diameter of the ZnO microdots was observed to be similar regardless of the substrate temperature, with diameters of 45.6 μm and 43.8 μm at room temperature and 60 °C, respectively.

Given the proportionality between contact line pinning probability and solution concentration, it is reasonable to assume that dilution is a plausible approach to decrease the size of the inkjet-printed microdots. Although other mechanisms may have contributed, reducing the concentration of the solution resulted in a decrease in droplet size to some extent (Fig. S8). In addition, substrate surface energy is a critical factor for the morphology formation of microdots, as it can affect the droplet ink shape and internal fluid behavior. To control the surface energy without significantly affecting other properties, the ITO surface was treated with OTS SAM. Note that the untreated ITO substrate retains a relatively high surface energy compared to its UV-ozone treated counterpart. The OTS develops low surface energy conditions for a high contact angle of ZnO ink, maintaining a minimized interfacial contact area with substrates during the drying process, which is favorable for miniaturization. As shown in Fig. 3b, **d**, **f**, and **h**, ZnO microdots deposited on the ITO/OTS exhibited a diameter of 5.5 μm which is much smaller than that seen on the pristine ITO (38.6 μm). The suppressed coffee-ring effect contributes to the uniform distribution of solutes during the solidification process, forming a smooth coin-shaped structure with a height of approximately 70 nm (Fig. 3h).

The key to miniaturizing ZnO microdots is to keep the contact line

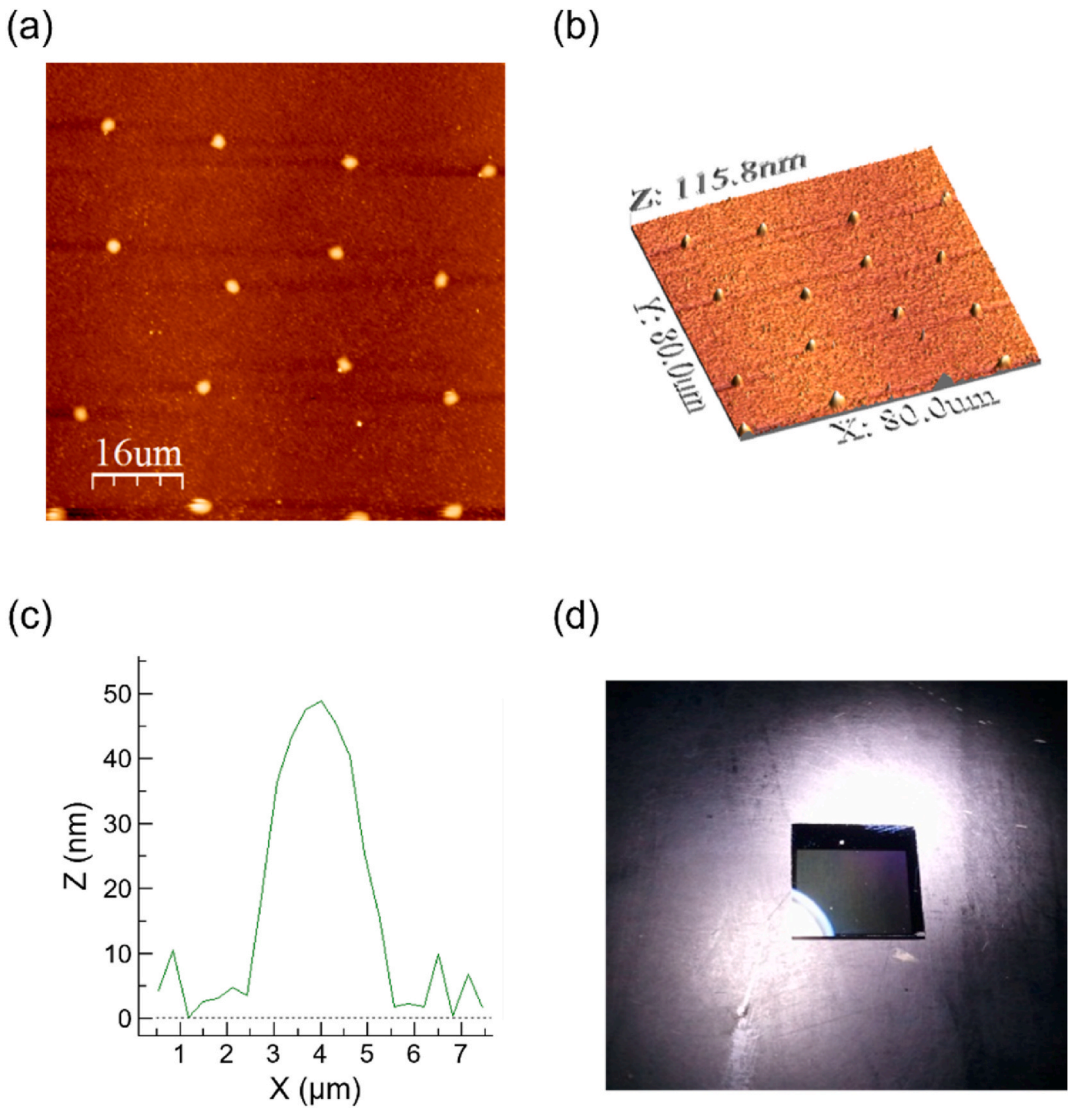

Fig. 4. The AFM (a) 2D, (b) 3D images, and (c) corresponding line profile of inkjet-printed ZnO microdot array deposited on the ITO/ODTS substrate. (d) Inkjet-printed ZnO microdot array on OTS treated SiO_2 substrate. To facilitate the observation of optical interference effects, a Si/SiO_2 substrate was used instead of a glass/ITO substrate.

unpinned as much as possible until the complete evaporation. The size of microdots can be effectively reduced by depositing a low concentration solution with a low surface energy substrate to form near-spherical droplets with minimal contact area. By carefully controlling the solution concentration and substrate surface energy, ZnO microdots have a diameter of around 3 μm and a thickness of 50 nm, representing one of

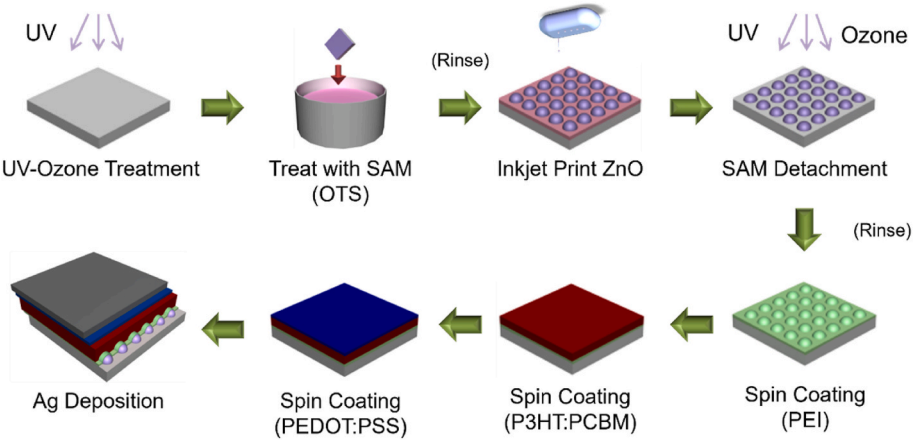

Fig. 5. Step-by-step device fabrication process of organic solar cells with inkjet-printed ZnO microdots.

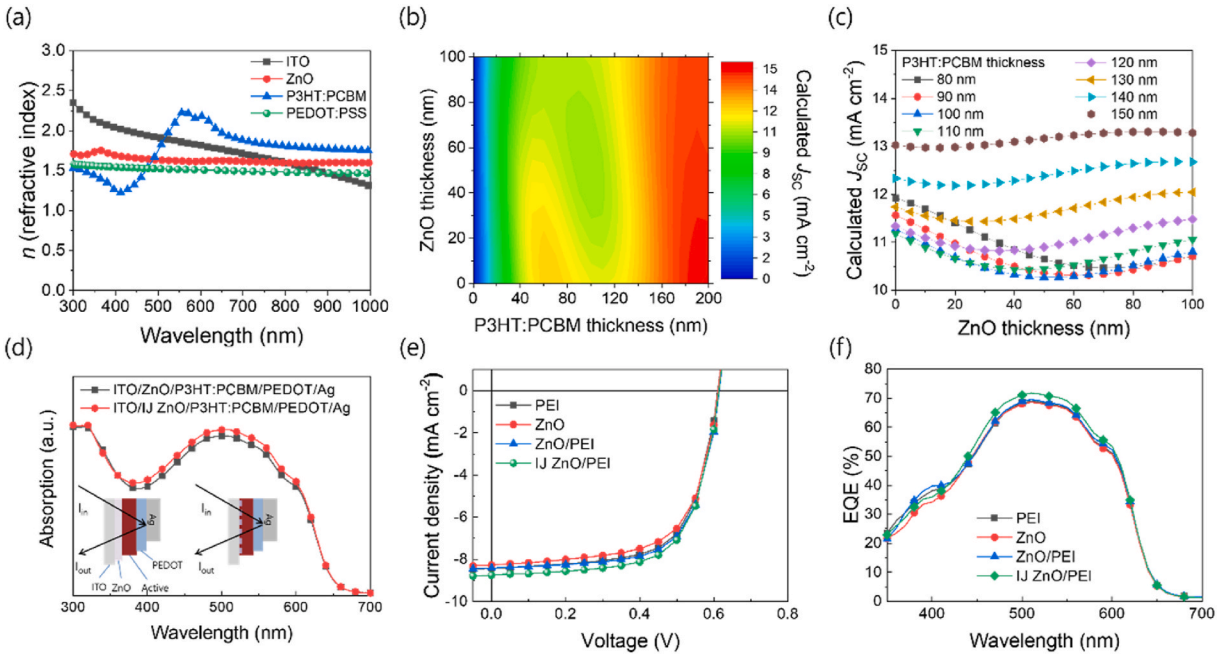

Fig. 6. (a) Refractive indices of ITO, ZnO, P3HT:PCBM, and PEDOT:PSS. (b) Simulated J_{SC} of organic solar cell with various ZnO and P3HT:PCBM thicknesses. (c) Dependence of the calculated J_{SC} on the ZnO layer thickness. (d) Total absorption in the cell through normal incidence reflectance measurements. Inset indicates the schematic illustrations of reflectance measurements for devices with and without inkjet-printed ZnO microdot array. (e) *J-V* characteristics and (f) corresponding EQE spectra of the P3HT:PCBM organic solar cells with PEI, ZnO, ZnO/PEI, and inkjet-printed ZnO/PEI ETLs.

the smallest microstructures in inkjet printing (Fig. 4). The thickness of the microdots ranged from 50 to 80 nm. Note that the irregular spacing between droplets results from the low concentration, causing evaporating droplets to nucleate randomly. Using smaller capacity cartridges (e.g., 1 pL) may decrease droplet size, yet it could lead to instability in jetting. Fig. 4d demonstrates the light scattering due to the presence of ZnO microdot arrays deposited on the OTS treated Si/SiO_2 substrate. Note that Si/SiO_2 substrates were used instead of glass/ITO substrates to facilitate visual observation of the optical interference effect. A photo of the ZnO microdot arrays printed on the ITO substrate is shown in Fig. S9. For the surface of ZnO microdots, the morphology was characterized by smooth curvature, lacking distinctive structures such as nanowires, granules, and nanoridges (Fig. S10). X-ray diffraction patterns revealed the sol-gel derived ZnO possesses polycrystalline feature with a hexagonal wurzite structure and a preferred orientation along the (002) basal plane (Fig. S11).

We now turn to the application of ZnO microdots for organic solar cells. Although ZnO is widely used as an ETL due to its low work function and high electron mobility, ZnO microdot arrays contain uncovered areas on the substrate, making it necessary to use another cathode interface layer for the ITO electrode to function as an electron-selective contact. To address this issue, we introduced PEI as the cathode interface layer. The process of fabricating a device is briefly described as follows (Fig. 5): first, an OTS SAM is first chemisorbed onto an ITO substrate, followed by inkjet printing of ZnO microdot arrays. The remaining SAM is then removed from the surface by UV-ozone treatment, and the surface is cleaned and coated with PEI. Then, a bulk heterojunction layer containing P3HT and PCBM as donor and acceptor, respectively, is introduced as the photoactive layer. PEDOT:PSS and Ag are then deposited to complete the device fabrication.

Given the large number of voids and the much thicker than optimized thickness, ZnO arrays are expected to be more useful for optical rather than electron transport gains. Fig. 6a plots the refractive indices of component materials used in organic solar cells. The refractive index values are taken from the database [46]. The results are in good agreement with experimental measurements of the refractive index and extinction coefficient of ZnO (Fig. S12). Since ZnO has less optical absorption in the visible region and a lower refractive index than P3HT:PCBM, it can refract light incident on the ITO substrate, which is expected to increase the effective optical absorption length in organic solar cells. As presented in Fig. 6b, we performed optical simulations based on the transfer matrix formalism with respect to thicknesses of the ZnO and P3HT:PCBM layers [47]. For photoactive layer thicknesses above 120 nm in P3HT:PCBM, both the presence and absence of ZnO microdots are beneficial for photocurrent compared to that of ZnO thin films, which can be attributed to increased absorption in the photoactive layer [Fig. 6c].

To validate the assumptions, the total absorption in the devices was measured in a reflection geometry with and without ZnO microdots (Fig. 6d). As a result, organic solar cells containing ZnO microdots showed a weak but distinct increase in internal absorption. Finally, organic solar cells with different ETL configurations were fabricated and characterized. The photovoltaic parameters of the devices are summarized in Table 2. Fig. 6e exhibits the *J–V* characteristics of the devices

Table 2
Photovoltaic performance parameters of organic solar cells.

Photoactive materials	ETL	V_{OC} (V)	J_{SC}[a] (mA cm^{-2})	J_{SC}[b] (mA cm^{-2})	FF (%)	PCE (%)
P3HT:PCBM	PEI	0.61	8.39	8.47	0.66	3.38
	ZnO	0.61	8.27	8.36	0.66	3.33
	ZnO/PEI	0.61	8.41	8.56	0.67	3.46
	IJ ZnO/PEI	0.61	8.86	8.81	0.66	3.54
PTB7-Th:PCBM	ZnO/PEI	0.79	15.41	15.38	0.73	8.85
	IJ ZnO/PEI	0.79	15.72	15.71	0.72	9.04
PM6:Y6	ZnO/PEI-mNBr	0.83	24.63	24.48	0.75	15.25
	IJ ZnO/PEI-mNBr	0.82	25.21	24.96	0.75	15.61

[a] The values are extracted from the *J–V* characteristics.
[b] The values are calculated from the EQE spectra.

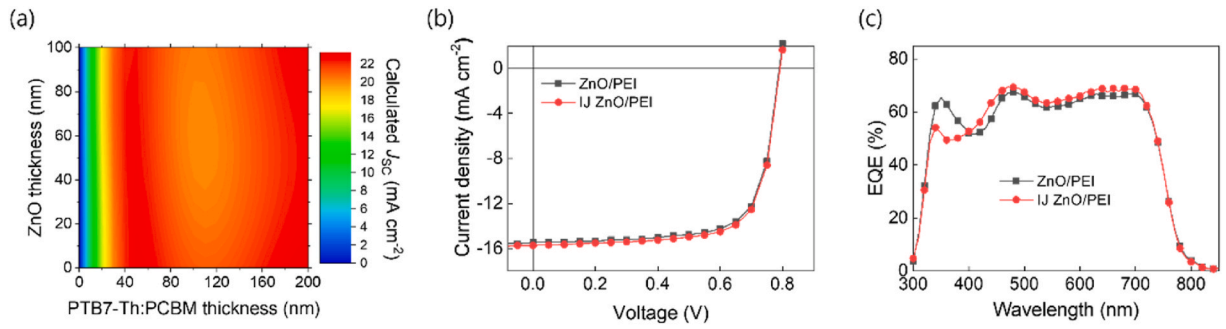

Fig. 7. (a) Simulated J_{SC} values of PTB7-Th:PCBM organic solar cells as a function of ZnO thicknesses. (b) *J-V* characteristics and (c) corresponding EQE spectra of the devices with ZnO/PEI and inkjet-printed ZnO/PEI ETLs.

measured under standard illumination conditions. For devices based on PEI or ZnO, we obtained moderate power conversion efficiencies (PCEs) of 3.38% and 3.33%, respectively, which are similar to previous results. Compared to an ETL in a single layer configuration, the ZnO/PEI bilayer device showed improved photovoltaic parameters, including an open circuit voltage V_{OC} of 0.61 V, a short circuit current density (J_{SC}) of 8.41 mA cm^{-2}, and a fill factor (FF) of 0.67, resulting in a PCE of 3.46%. This improvement is attributed to the reduction of the work function of ZnO by PEI (Fig. S13). The device with inkjet-printed ZnO microdot arrays showed the highest efficiency of 3.54%, with a particularly high J_{SC} value of 8.86 mA cm^{-2}, along with V_{OC} of 0.61 V and FF of 0.66%, reflecting the increased absorption of light in the photoactive layer. The increased total absorption along with current density values were consistent with the EQE spectra shown in (Fig. 6f). The optical effects produced by ZnO microdot arrays depend on the geometry of the microstructure. Interestingly, for ZnO microdots with coffee ring features, there is a weak contribution to the current, which may be due to the presence of curved surfaces at the ring edges. However, the coffee ring structure is difficult to control, which limits the widespread application of ZnO microdots. In contrast, very large and thick ZnO microdots were found to exert adverse effects on the FF of the devices. (Fig. S14 and Table S1). In addition, the low density of the ZnO microdot arrays also diminishes the optical effect. Thus, it can be concluded that the fabrication of structures with high density and large surface curvature is important.

We extended the use of ZnO microdot arrays to organic solar cells based on poly[4,8-bis(5-(2-ethylhexyl)thiophen-2-yl)benzo[1,2-*b*:4,5-*b*′]dithiophene-co-3-fluorothieno [3,4-b]thiophene-2-carboxylate] (PTB7-Th):PCBM as the photoactive layer. The simulation results indicate that the dependence on ZnO thickness is not significant for the PTB7-Th:PCBM system as the thickness approaches 100 nm (Fig. 7a and S15). Similar to the experimental observations in the P3HT:PCBM

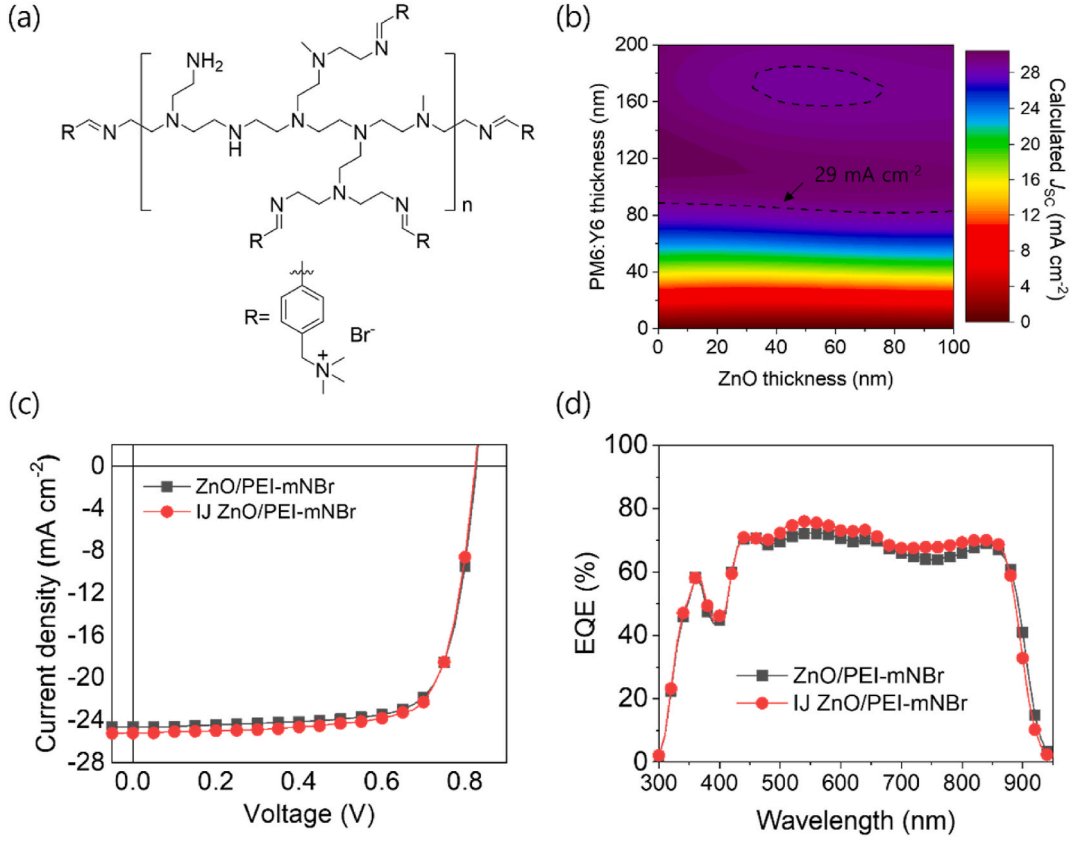

Fig. 8. (a) Chemical structure of PEI-mNBr. (b) Simulated J_{SC} values of PM6:Y6 organic solar cells depending on ZnO thicknesses. (c) *J-V* characteristics and (d) corresponding EQE spectra of the PTB7-Th:PCBM organic solar cells with ZnO/PEI-mNBr and inkjet-printed ZnO/PEI-mNBr ETLs.

system, it was found that more light can be absorbed by PTB7-Th:PCBM inside the device containing the ZnO microdot arrays (Fig. S16). Fig. 7b and **c** compare the *J–V* characteristics and EQE spectra of the devices. The optimized reference device with ZnO/PEI ETL gave a PCE of 8.85%, with a V_{OC} of 0.79 V, a J_{SC} of 15.41 mA cm^{-2}, and a FF of 0.73. In contrast, the ZnO microdot array-based device outperformed the reference device, exhibiting a higher PCE of 9.04% with a V_{OC} of 0.79 V, a J_{SC} of 15.72 mA cm^{-2}, and a FF of 0.72 (Table 2). The increased photocurrent value is responsible for the resulting PCE, demonstrating the effectiveness of the ZnO microdots while the thickness and/or surface morphology of the photoactive layer may influence the optical field distribution and therefore EQE spectra (Fig. S17). To further explore the applicability of ZnO microdot arrays in organic solar cells, we adopted a high-performing non-fullerene acceptor-based photovoltaic blend of PM6:Y6. While PM6:Y6 photoactive layer-based organic solar cells show stable high efficiency in ZnO ETL systems, the polyethyleneimine (PEI) layer can cause poor interfacial properties through undesirable chemical interactions with non-fullerene acceptor (Fig. S18) [48]. To mitigate this problem, we adopted a polymer electrolyte, PEI-mNBr, as a cathode interface layer with suppressed chemical reactivity (Fig. 8a) [49]. The PEI-mNBr provided a chemically stable nature along with broad work function tunability, possibly demonstrating high-efficiency non-fullerene acceptor organic solar cells. Notably, for PM6:Y6 organic solar cells, the current enhancement was more pronounced in PM6:Y6, similar to the simulation results (Fig. 8b and S19). The IJ ZnO/PEI-mNBr ETL exhibited a high PCE of 15.61%, which is higher than the control device with ZnO/PEI-mNBr (15.25%) (Fig. 8c, **d**, and Table 2). These results suggest that inkjet-printed ZnO microdot arrays can be expected to provide greater improvements in high-efficiency, low-bandgap photoactive material systems.

4. Conclusions

In conclusion, we have investigated the inkjet printing of ZnO microdots and their morphologies depending on the drying process. The inkjet printing process was comprehensively analyzed, demonstrating the production of high-resolution ZnO microdots with a suppressed coffee-ring effect. The study of the solidification behavior of inkjet-printed ZnO droplets elucidated the influence of Marangoni flow, capillary flow, and nucleation on droplet morphology and microstructure formation. It was found that the substrate temperature and surface energy affect droplet geometry and the drying process, which significantly impacts the morphology of the deposited microdots. We further incorporated the ZnO microdot arrays into organic solar cells to alter the light path length, resulting in enhanced internal absorption and photovoltaic performance. The devices with inkjet-printed ZnO microdots had higher PCEs of 3.54%, 9.04%, and 15.61% for the P3HT:PCBM, PTB7-Th:PCBM, and PM6:Y6 systems, respectively, compared to 3.46%, 8.85%, and 15.25% for the reference device. This work highlights the potential of inkjet-printed ZnO microdots for enhancing the performance of organic solar cells and underlines the significance of comprehending fluid behavior and drying mechanisms in inkjet printing processes for functional device fabrication.

Declaration of competing interest

The authors declare that they have no known competing financial interests or personal relationships that could have appeared to influence the work reported in this paper.

Acknowledgements

This work was supported by the National Research Foundation of Korea (NRF) grant funded by the Korea government (MSIT) (RS-2023-00278803), and the Korea Research Institute of Chemical Technology (KRICT-KS2422-10). This research was also supported by the GIST RISE grant funded by the GIST in 2024.

Appendix A. Supplementary data

Supplementary data to this article can be found online at https://doi.org/10.1016/j.jmrt.2024.07.084.

References

[1] Calvert P. Inkjet printing for materials and devices. Chem Mater 2001;13:3299–305.
[2] De Gans BJ, Duineveld PC, Schubert US. Inkjet printing of polymers: state of the art and future developments. Adv Mater 2004;16:203–13.
[3] Singh M, Haverinen HM, Dhagat P, Jabbour GE. Inkjet printing-process and its applications. Adv Mater 2010;22:673–85.
[4] Zhan Z, An J, Wei Y, Tran VT, Du H. Inkjet-printed optoelectronics. Nanoscale 2017;9:965–93.
[5] Cai G, Cheng X, Layani M, Tan AWM, Li S, Eh ALS, et al. Direct inkjet-patterning of energy efficient flexible electrochromics. Nano Energy 2018;49:147–54.
[6] Tekin E, Smith PJ, Schubert US. Inkjet printing as a deposition and patterning tool for polymers and inorganic particles. Soft Matter 2008;4:703–13.
[7] Bao B, Li M, Li Y, Jiang J, Gu Z, Zhang X, et al. Patterning fluorescent quantum dot nanocomposites by reactive inkjet printing. Small 2015;11:1649–54.
[8] Thesen MW, Ruttloff S, Limberg RPF, Vogler M, Nees D, Grützner G. Photo-curable resists for inkjet dispensing applied in large area and high throughput roll-to-roll nanoimprint processes. Microelectron Eng 2014;123:121–5.
[9] Abbel R, Teunissen P, Rubingh E, van Lammeren T, Cauchois R, Everaars M, et al. Industrial-scale inkjet printed electronics manufacturing-production up-scaling from concept tools to a roll-to-roll pilot line. Transl Mater Res 2014;1:15002.
[10] Fu S, Tao J, Wu W, Sun J, Li F, Li J, et al. Fabrication of large-area bimodal sensors by all-inkjet-printing. Adv Mater Technol 2019;4:1800703.
[11] Cai G, Darmawan P, Cheng X, Lee PS. Inkjet printed large area multifunctional smart windows. Adv Energy Mater 2017;7:1602598.
[12] Yan K, Li J, Pan L, Shi Y. Inkjet printing for flexible and wearable electronics. Apl Mater 2020;8:120705.
[13] Huang TT, Wu W. Inkjet-printed wearable nanosystems for self-powered technologies. Adv Mater Interfaces 2020;7:2000015.
[14] Gao M, Li L, Song Y. Inkjet printing wearable electronic devices. J Mater Chem C Mater 2017;5:2971–93.
[15] Liu Y, Zhu H, Xing L, Bu Q, Ren D, Sun B. Recent advances in inkjet-printing technologies for flexible/wearable electronics. Nanoscale 2023;15:6025–51.
[16] Du X, Wankhede SP, Prasad S, Shehri A, Morse J, Lakal N. A review of inkjet printing technology for personalized-healthcare wearable devices. J Mater Chem C 2022;10:14091–115.
[17] Lo LW, Zhao J, Wan H, Wang Y, Chakrabartty S, Wang C. An inkjet-printed PEDOT:PSS-based stretchable conductor for wearable health monitoring device applications. ACS Appl Mater Interfaces 2021;13:21693–702.
[18] Patil P, Patil S, Kate P, Kulkarni AA. Inkjet printing of silver nanowires on flexible surfaces and methodologies to improve the conductivity and stability of the printed patterns. Nanoscale Adv 2021;3:240–8.
[19] Yoshioka Y, Jabbour GE. Desktop inkjet printer as a tool to print conducting polymers. Synth Met 2006;156:779–83.
[20] Wang JZ, Zheng ZH, Li HW, Huck WTS, Sirringhaus H. Dewetting of conducting polymer inkjet droplets on patterned surfaces. Nat Mater 2004;3:171–6.
[21] Kholghi Eshkalak S, Chinnappan A, Jayathilaka WADM, Khatibzadeh M, Kowsari E, Ramakrishna S. A review on inkjet printing of CNT composites for smart applications. Appl Mater Today 2017;9:372–86.
[22] Torrisi F, Hasan T, Wu W, Sun Z, Lombardo A, Kulmala TS, et al. Inkjet-printed graphene electronics. ACS Nano 2012;6:2992–3006.
[23] Gorter H, Coenen MJJ, Slaats MWL, Ren M, Lu W, Kuijpers CJ, et al. Toward inkjet printing of small molecule organic light emitting diodes. Thin Solid Films 2013;532:11–5.
[24] Haverinen HM, Myllylä RA, Jabbour GE. Inkjet printing of light emitting quantum dots. Appl Phys Lett 2009;94:073108.
[25] Yang P, Zhang L, Kang DJ, Strahl R, Kraus T. High-resolution inkjet printing of quantum dot light-emitting microdiode arrays. Adv Opt Mater 2020;8:1901429.
[26] Li Y, Lan L, Sun S, Lin Z, Gao P, Song W, et al. All inkjet-printed metal-oxide thin-film transistor array with good stability and uniformity using surface-energy patterns. ACS Appl Mater Interfaces 2017;9:8194–200.
[27] Liu X, Tarn TJ, Huang F, Fan J. Recent advances in inkjet printing synthesis of functional metal oxides. Particuology 2015;19:1–13.
[28] Shi J, Cagney N, Tatum J, Condie A, Rafael Castrejon-Pita J. Jetting and droplet formation of particle-loaded fluids. Phys Fluids 2024;36:017119.
[29] Zhong Y, Fang H, Ma Q, Dong X. Analysis of droplet stability after ejection from an inkjet nozzle. J Fluid Mech 2018;845:378–91.
[30] Lohse D. Fundamental fluid dynamics challenges in inkjet printing. Annu Rev Fluid Mech 2022;54:349–82.
[31] Li D, Li H, Yang G, Cao Y, Huang B, Wu X, et al. Mechanisms of inkjet printing in a liquid environment. J Fluid Mech 2022;948:A40.
[32] Derby B. Inkjet printing of functional and structural materials: fluid property requirements, feature stability, and resolution. Annu Rev Mater Res 2010;40:395–414.

[33] De Gans BJ, Schubert US. Inkjet printing of well-defined polymer dots and arrays. Langmuir 2004;20:7789–93.
[34] Hu H, Larson RG. Marangoni effect reverses coffee-ring depositions. J Phys Chem B 2006;110:7090–4.
[35] Minemawari H, Yamada T, Matsui H, Tsutsumi JY, Haas S, Chiba R, et al. Inkjet printing of single-crystal films. Nature 2011;475:364–7.
[36] Yunker PJ, Still T, Lohr MA, Yodh AG. Suppression of the coffee-ring effect by shape-dependent capillary interactions. Nature 2011;476:308–11.
[37] Peng X, Yuan J, Shen S, Gao M, Chesman ASR, Yin H, et al. Perovskite and organic solar cells fabricated by inkjet printing: progress and prospects. Adv Funct Mater 2017;27:1703704.
[38] Liu Y, Li F, Xu Z, Zheng C, Guo T, Xie X, et al. Efficient all-solution processed quantum dot light emitting diodes based on inkjet printing technique. ACS Appl Mater Interfaces 2017;9:25506–12.
[39] Mattana G, Loi A, Woytasik M, Barbaro M, Noël V, Piro B. Inkjet-printing: a new fabrication technology for organic transistors. Adv Mater Technol 2017;2:1700063.
[40] Huber B, Popp PB, Kaiser M, Ruediger A, Schindler C. Fully inkjet printed flexible resistive memory. Appl Phys Lett 2017;110:143503.
[41] Moya A, Gabriel G, Villa R, Javier del Campo F. Inkjet-printed electrochemical sensors. Curr Opin Electrochem 2017;3:29–39.
[42] Cinquino M, Prontera CT, Zizzari A, Giuri A, Pugliese M, Giannuzzi R, et al. Effect of surface tension and drying time on inkjet-printed PEDOT:PSS for ITO-free OLED devices. J Sci: Adv Mater Devices 2022;7:100394.
[43] Yakovlev AV, Milichko VA, Pidko EA, Vinogradov VV, Vinogradov AV. Inkjet printing of TiO2/AlOOH heterostructures for the formation of interference color images with high optical visibility. Sci Rep 2016;6:37090.
[44] Kant C, Shukla A, McGregor SKM, Lo SC, Namdas EB, Katiyar M. Large area inkjet-printed OLED fabrication with solution-processed TADF ink. Nat Commun 2023;14:7220.
[45] Li Y, Yang Q, Li M, Song Y. Rate-dependent interface capture beyond the coffee-ring effect. Sci Rep 2016;6:24628.
[46] Polyanskiy MN. Refractiveindex.info database of optical constants. Sci Data 2024;11:94.
[47] Burkhard GF, Hoke ET, McGehee MD. Accounting for interference, scattering, and electrode absorption to make accurate internal quantum efficiency measurements in organic and other thin solar cells. Adv Mater 2010;22:3293–7.
[48] Hu L, Liu Y, Mao L, Xiong S, Sun L, Zhao N, et al. Chemical reaction between an ITIC electron acceptor and an amine-containing interfacial layer in non-fullerene solar cells. J Mater Chem A 2018;6:2273–8.
[49] Kyeong M, Lee J, Daboczi M, Stewart K, Yao H, Cha H, et al. Organic cathode interfacial materials for non-fullerene organic solar cells. J Mater Chem A 2021;9:13506–14.